Catalysis Letters (2024) 154:2265–2274
https://doi.org/10.1007/s10562-023-04385-0

Enhanced Photocatalytic Performance of Z-Scheme Design of $Bi_2O_2CO_3$/Ag/g-C_3N_4 Photocatalyst

Jingjing Zheng[1] · Guoxia Liu[1] · Xiaozheng Feng[1] · Zhengbo Jiao[2]

Received: 22 May 2023 / Accepted: 6 June 2023 / Published online: 11 October 2023

Abstract

The g-C_3N_4/Ag/$Bi_2O_2CO_3$ nanosheets were synthesized using a mixture of precursors containing melamine and nitrates of silver and bismuth through a simple one-pot synthesis strategy. In the presence of ammonium nitrate, g-C_3N_4/Ag/$Bi_2O_2CO_3$ composite catalysts with different silver mass ratios were prepared, and the photodegradation performance of the composite samples was evaluated by photodegradation of tetracycline hydrochloride (TC) under simulated solar light irradiation. The synthesized composites were characterized by XPD, XPS, FT-IR, TEM, UV–vis DRS and PL. It was found that the g-C_3N_4/Ag/$Bi_2O_2CO_3$ catalyst with Ag mass ratio of 4% exhibited the highest catalytic activity, and the degradation effect was more than 9 times that of pure C_3N_4 and nearly 5 times that of g-C_3N_4/$Bi_2O_2CO_3$.In addition, cyclic experiments showed that g-C_3N_4/Ag/$Bi_2O_2CO_3$ composites had certain stability. The photocatalytic performance of the g-C_3N_4/Ag/$Bi_2O_2CO_3$ composites was attributable to the heterogeneous junction of $Bi_2O_2CO_3$ and g-C_3N_4 and the surface plasmon resonance effect (SPR) of Ag nanoparticles. The energy levels of $Bi_2O_2CO_3$ and g-C_3N_4 were properly matched to form a heterojunction, which promoted the separation and transfer of photogenerated electrons and holes, thereby improving the photocatalytic performance. The Ag surface plasmon resonance (SPR) effect not only accelerated the separation and transmission of electron–hole pairs, but also enhanced the absorption of visible light. Finally, based on the above basis, a possible photocatalytic mechanism was proposed.

Graphical Abstract

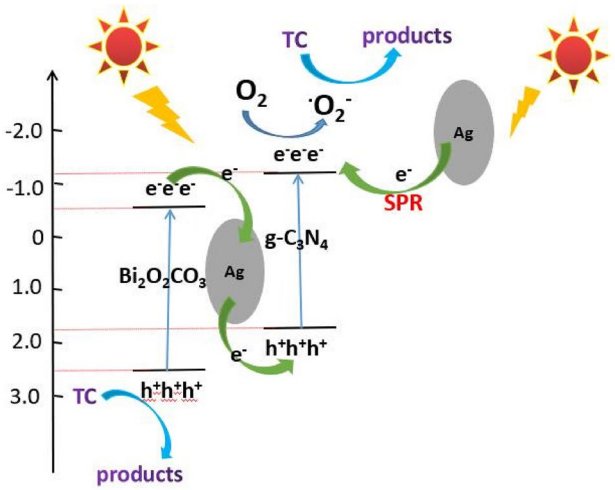

Keywords Z-scheme-heterojunction · Ag · $Bi_2O_2CO_3$ · g-C_3N_4

Extended author information available on the last page of the article

1 Introduction

With the development of industry, a large amount of industrial waste was discharged into the water, which was extremely harmful to the environment [1, 2]. To address these hazards, many solutions had been developed, such as membrane filtration [3], chemical oxidation [4], and microbial degradation [5]. However, the use of these methods to treat contamination was unsatisfactory due to secondary pollution and high cost. Therefore, finding a green and efficient method of treating pollutants had become an urgent matter. Recently, the use of semiconductor materials to degrade pollutants using solar energy had attracted great attention [6, 7]. Graphite phase phase carbonitride (g-C_3N_4) was a low cost, high stability metal-free catalyst. The forbidden band width of g-C_3N_4 was about 2.7 eV, which was much lower than the forbidden band width of ZnO and TiO_2, and can absorb visible light for catalytic degradation reaction [8–10]. Based on the above reasons, g-C_3N_4 had caused great concern. However, g-C_3N_4 also had serious shortcomings. Most of the conventionally synthesized g-C_3N_4 was a massive structure, and the bulk g-C_3N_4 had the disadvantages of small specific surface area, fast internal photo-generated carrier current and low photocatalytic activity [11, 12]. In order to change the shortcomings of bulk g-C_3N_4, it was proposed to manufacture g-C_3N_4 with ultra-thin nanosheet structure. In photocatalysis, semiconductor materials with nanosheet structure had rich activity due to relatively large surface area and ultra-thin thickness. Generally, methods for preparing nanosheet structures include thermal oxidation etching and ultrasonic assisted liquid stripping [13, 14]. However, both methods had certain disadvantages. Thermal oxidation etching caused a large amount of interface defects in the semiconductor material, and the yield of ultrasonic assisted liquid stripping was relatively low. Recently, a route for synthesizing g-C_3N_4 nanosheets using chemical blowing had been reported [15, 16]. In order to increase the activity of g-C_3N_4, it was necessary to modify g-C_3N_4. Common modification methods included doping modification, semiconductor recombination, morphology control etc. [17–20]. In recent years, in the field of photocatalysis, in addition to g-C_3N_4, Bi-based semiconductor materials had also been greatly explored and developed [21–23]. Bismuth carbonate ($Bi_2O_2CO_3$) was a typical Aurivillius/Sillén phase compound in Bi-based compounds. Due to its unique photocatalytic activity, low cost and stability, it had been widely concerned [24–27]. $Bi_2O_2CO_3$ had a unique layered structure, which was composed of alternating $[Bi_2O_2]^{2+}$ and CO_3^{2-}, which could accelerate the transfer of active substances between layers and improve photocatalytic activity [28]. However, the band gap of $Bi_2O_2CO_3$ was 2.8–3.5 eV, which could only be corresponding under ultraviolet light. In order to improve the deficiency of g-C_3N_4 and $Bi_2O_2CO_3$, and to make good use of the advantages of the two semiconductor materials, it was preferred to modify g-C_3N_4 with $Bi_2O_2CO_3$. A heterojunction can be formed between $Bi_2O_2CO_3$ and g-C_3N_4, which not only broadens the light absorption range, but also accelerates the transfer of photogenerated carriers [27]. Among these heterojunction materials, Z-scheme heterojunctions exhibited the dual advantages of suppression of recombination of electron-holepairs and reserving high redox ability for both semiconductors [29, 30]. In particular Z-scheme heterojunction photocatalysts with noble metals as bridges showed better photocatalytic performance [31, 32]. Due to the surface plasmon resonance effect (SPR) of the noble metal[33], on the one hand, the light absorption range could be broadened, and on the other hand, it could suppress the superposition electron–hole pair recombination in the semiconductor catalyst, thereby causing the photocatalytic activity of the catalyst to be greatly improved [34, 35]. Among many precious metals, Ag was selected as a load metal due to its low price.

In view of practical application, the preparation method was of great importance. In this work, a simple one-pot synthesis strategy was chosen to synthesize Z-scheme g-C_3N_4/Ag/$Bi_2O_2CO_3$ materials. Compared with other preparation methods, the method reduced the cumbersome steps and shortened the synthesis cycle, which provided a possibility for practical application. The performance of the composite photocatalyst was evaluated using tetracycline hydrochloride (TC) degradation. Compared with pure g-C_3N_4 and g-C_3N_4/$Bi_2O_2CO_3$, the photocatalytic activity of the synthesized g-C_3N_4/Ag/$Bi_2O_2CO_3$ was significantly improved. Finally, based on the capture agent experiments, the reaction mechanism of the composite was inferred.

2 Experimental Section

All chemicals were reagent grade and used directly withoutany further purification. Chemical agents, Melamine and bismuth nitrate pentahydrate were purchased from Shanghai sinopharm chemical reagent co., LTD., China. Silver nitrate was obtained from tianjin fengchuan chemical reagent technology co., LTD., China. Ammonium nitrate was purchased from Shanghai reagent co., LTD.,China. All the water used in the experiment was deionized water, and the whole experiment process was carried out under the pressure of greenhouse.

A g-C_3N_4/Ag/$Bi_2O_2CO_3$ photocatalyst sample was synthesized by a one-step milling roasting method. In a typical process, 3.0 g of melamine, 0.45 g of NH_4NO_3, 0.032 g of $Bi(NO_3)_3{\cdot}5H_2O$, and a portion of silver nitrate

are thoroughly milled in a mortar for 30 min at room temperature. The ground mixture was placed in a crucible and the crucible was placed in a muffle furnace. It was heated to 550 °C in a muffle furnace at a heating rate of 5 °C/min, and then held for 2 h. After the muffle furnace was naturally cooled to room temperature, a yellow solid was obtained, which was ground to a fine powder for use. The catalyst used in the study was abbreviated as x wt% CN/Ag/BiOC, where x represented the mass concentration of Ag in the sample. Moreover, a series of composite CN/Ag/BiOC samples with different contents of $Bi_2O_2CO_3$ were synthesized by the same method. These catalysts were abbreviated as x wt% CN/Ag/BiOC-y, where y represented the amount of $Bi_2O_2CO_3$ in the catalyst (wt %).

X-ray powder diffraction (XRD) patterns of the samples were examined on the Bruker D8 X-ray diffraction instrument with CuKa gamma ray (λ = 1.5418A), and the CuKa ray scanning range is 5° to 90°. High resolution transmission electron microscopic (HRTEM) mages were acquired with FEI-Tecnai-G20 TEM microscope. The chemical composition and chemical state of CN/Ag/BiOC complex were analyzed by X ray photoelectron spectroscopy (XPS) on Escalab 250Xi X-ray photoelectron spectrometer with Al Ka excitation source. The FT-IR experiment was carried out on a NiCOLET 380 type FT-IR spectrometer (hermo Electron Corporation) using KBr as the background, and the scanning range was selected to be 4000–400 cm^{-1}. Diffuse reflectance spectra were recorded using a TU-1950 dual-beam UV spectrophotometer with barium sulfate as the background and a wavelength range of 200 nm to 800 nm. Photoluminescence (PL) spectra were performed on a FL970 fluorescence spectrophotometer with an excitation wavelength of365 nm. The photocurrent response under simulated solar light irradiation was recorded with a CHI-660D electrochemical workstation in a sandwich-type configuration, a Pt slice as the counter electrode, a saturated calomel electrode (SCE) as the reference, and 0.1 M Na_2SO_4 solution as electrolyte. A 300W xenon arc lamp equipped with a simulated solar light filter (HSX-F300, Beijing NBeT Technology Co., Ltd) calibrated to 100 mW/cm^2, which was measured with a radiometer (CEL-NP2000, Beijing Au-light Co., Ltd), employed as the light source. Electrochemical impedance spectroscopy (EIS) Nyquist plots were obtained at 0.6 V with small AC amplitude of 5 mV in the frequency range of 0.1–10^5 Hz. All experiments were carried out under ambient conditions.

In the experimental setup, a 500 W xenon lamp was employed as a light source. The photocatalytic activity of the CN/Ag/BiOC sample was determined by degrading the simulated pollutant tetracycline (TC). The photodegradation reaction was carried out in a photochemical reactor. Before photodegradation, about 50 mg of catalyst was added to 50 ml of TC solution (1×10^{-4} mol·L^{-1}), and the solution was magnetically stirred in the dark for 3 h to reach the adsorption–desorption equilibrium between the catalyst and tetracycline. Then the solution was exposed to simulated solar light irradiation under magnetic stirring. During the degradation process, About 3 mL aliquot was periodically taken out from the reactor and centrifuged immediately every 10 min. The absorbance of the solution was then measured at 357 nm using a UV–Vis spectrophotometer (UV-2550, Shimadzu) to analyze the degradation of the TC solution. The formula for calculating the photocatalytic degradation efficiency was as follows:

$$\text{Photodegradation efficiency}(\%) = \left(C_0 - C_t\right)/C_0 \times 100\%$$

Where t represented time, C represented the concentration of TC, C_0 was the initial concentration of TC, and C_t was the concentration of TC at time t.

To test the stability of the catalyst sample, a sample reuse experiment was performed. The catalyst was washed with water and briefly sonicated before each interval of the experiment.

3 Results and Discussion

A simple synthesis process for the catalyst sample was shown in Fig. 1. Bismuth nitrate, silver nitrate and ammonium nitrate were encapsulated or adhered by melamine during mixing with melamine. During the calcination process, the melamine molecules were heat-shirked into a 2D carbon nitride layer, and the 2D carbon nitride layer was deposited to form a 3D g-C_3N_4. During the heating process, ammonium nitrate, bismuth nitrate and silver nitrate would decompose, releasing NH_3, NO, NO_2 and other gases. These gases acted as a template to accelerate the formation of the composite and made the material have a large number of pore structures. At the same time, metallic silver nanoparticles and solid $Bi_2O_2CO_3$ products appeared on the g-C_3N_4 nanosheets.

The crystal structures of the synthesized samples were analyzed by XRD diffraction pattern, as shown in Fig. 2. No

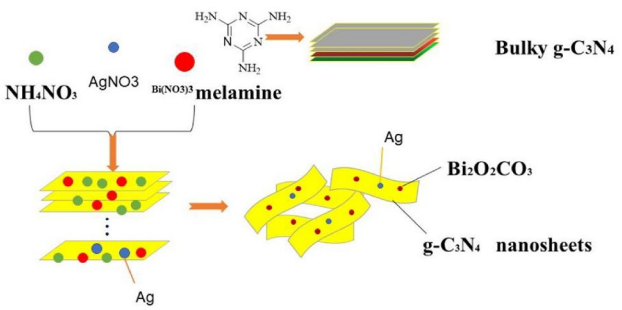

Fig. 1 Schematic depicting the process of CN/Ag/BiOC formation

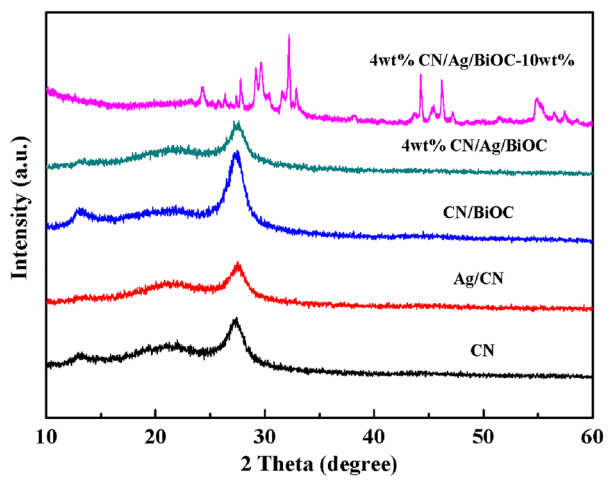

Fig. 2 The XRD patterns of pure g-C_3N_4, CN/Ag, CN/BiOC and the CN/Ag/BiOC nanocomposites

excess peak was found in the XRD pattern, indicating that the synthesized sample did not contain any impurities. In the XRD pattern of g-C_3N_4, there were two significant characteristic peaks at 13.4° and 27.4° [36]. The characteristic peak at 13.4° corresponded to the (100) diffractive surface of g-C_3N_4, which corresponded to the interplanar structural packing. The diffraction peak at 27.4° corresponded to the (002) crystal plane of g-C_3N_4, reflecting the interlayer deposition characteristics of the conjugated aromatic system. For the CN/BiOC composites, no diffraction peak corresponding to $Bi_2O_2CO_3$ was found, which may be caused by the relatively small amount of bismuth species in the synthesis. However, compared with the XRD pattern of pure g-C_3N_4 material, the diffraction intensity of the CN/BiOC material at 27.4° was greatly increased, which was sharper, indicating that the addition of Bismuth nitrate in the synthesis increased the crystallinity of the material. The XRD of CN/Ag/BOC composites with different contents of $Bi_2O_2CO_3$ were prepared in order to verify the presence of $Bi_2O_2CO_3$ in the composite. As shown in Fig. 2, it was obvious that the diffraction peaks of tetragonal phase $Bi_2O_2CO_3$ were found as the content of $Bi_2O_2CO_3$ is 10wt % [23]. No diffraction peak of Ag was found in the XRD patterns of CN/Ag/BiOC and Ag/CN materials, which may be caused by the relatively small amount of Ag species in the synthesis. The presence of Ag in the CN/Ag/BiOC samples was confirmed by the following TEM and XPS images.

The morphology and microstructure of the samples were investigated by the high-resolution transmission electron microscopy (HRTEM). As shown in Fig. 3, it could be observed in Fig. 3a that the synthesized CN/Ag/BiOC sample was a two-dimensional irregular layered nanosheet material and the bismuth species were well dispersed on the g-C_3N_4nanosheets. The attached small nanocrystals had a lattice fringe spacing of 0.372 nm, which could be ascribed to the (011) planes of tetragonal phase $Bi_2O_2CO_3$ [37] (Fig. 3b). In addition, the lattice fringe of d = 0.210 nm was measured to correspond to the (200) crystal plane of Ag [38], indicating metal Ag Nanoparticles were present in CN/Ag/BiOC samples.

The FT-IR spectroscopy was used to reveal the interfacial interaction between g-C_3N_4 and $Bi_2O_2CO_3$ in composite samples. The FT-IR spectra of g-C_3N_4 and different catalyst samples were shown in Fig. 4. It could be seen from the figure that g-C_3N_4 had a strong absorption band in the range of 900–1800 cm^{-1}, which could be ascribed to the C=N and aromatic C–N stretching vibration modes [39]. The band at 810 cm^{-1} was associated with the breathing modes of s-triazine ring system. The broad band at 3294 cm^{-1} could be assigned to the stretching mode of NH_2 or N–H groups. In the case of $Bi_2O_2CO_3$, the absorption peaks at about 551 and 848 cm^{-1} assigned to the stretching vibrations of the Bi-O and the bending mode of the CO_3^{2-} group, respectively, while the peaks at about 1400 cm^{-1} were associated with the stretching vibrations of C–O and C=O [40] respectively. The FTIR results of g-C_3N_4/Ag/$Bi_2O_2CO_3$ nanocomposites with

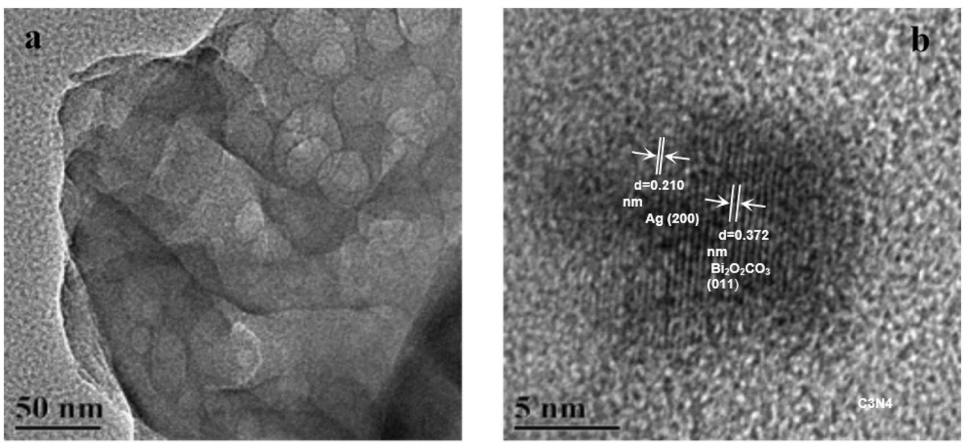

Fig. 3 TEM and HRTEM images of CN/Ag/BiOC nanocomposites

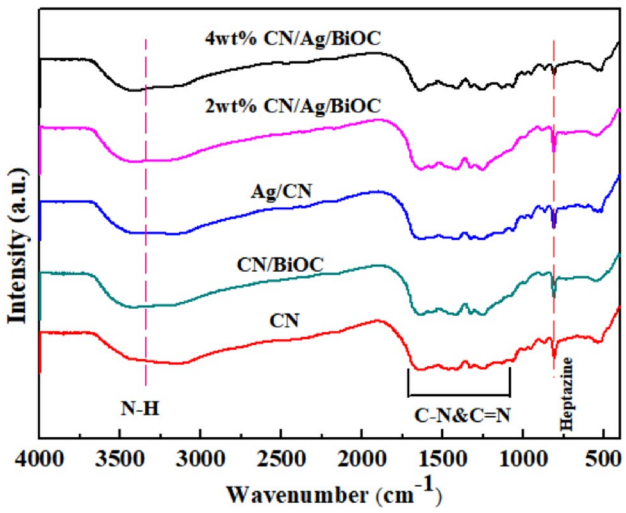

Fig. 4 FT-IR spectra of different samples: pure g-C_3N_4, Ag/CN, CN/BiOC and the CN/Ag/BiOC nanocomposites with different weight ratios

different weight ratios were very similar to those of pure g-C_3N_4, which may be due to the weak vibration mode of $Bi_2O_2CO_3$ and the strong IR response of g-C_3N_4.

The surface elemental composition and chemical state of the different elements in 4wt% CN/Ag/BiOC sample were investigated by XPS measurement. According to the Fig. 5a, the Bi 4f spectrum showed two distinct peaks at 158.9 and 164.3 eV, attributed to Bi $4f_{7/2}$ and Bi $4f_{5/2}$, yielding up shift of 0.7 and 0.9 eV in comparison with 158.2 and 163.4 eV for pure $Bi_2O_2CO_3$, respectively [41]. The upshift of binding energy may be attributed to the interaction between $Bi_2O_2CO_3$ and g-C_3N_4 [42]. As shown in Fig. 5b, the N 1 s XPS spectrum was devided into three component peaks at 398.3, 398.5, 400.2 eV, indexed as the C-N sp3 bonds, C = N sp2 bonds, and the interaction of g-C_3N_4 sheets with $Bi_2O_2CO_3$, respectively [43]. Figure 5c exhibited the Ag 3d XPS spectrum of 4wt %CN/Ag/BiOC and the binding energies of the Ag $3d_{3/2}$ and Ag $3d_{5/2}$ peaks as 373.8 and 367.8 eV were found respectively. According to this result, the Ag existed predominantly in the metallic form [44]. From Fig. 5d, it c0uld also be seen that the C 1 s peak was mainly devided into three peaks located at about 284.6, 287.5 and 288.3 eV, respectively. The peak located at 284.6 eV could be indexed as the signal of standard reference carbon [45].The peak located at 287.5 and 288.3 eV could be ascribed to C = N sp^2 bonds and the overlapping of sp^2 C atoms in carbonate in $Bi_2O_2CO_3$ and g-C_3N_4 [46]. In Fig. 5e, the XPS spectrum of O1s displayed two distinct peaks at 531.5 and 532.5 eV, corresponding to O^{2-}ions in the Bi-O bonds and the chemisorbed oxygen due to hydroxyl radicals [47]. According to these results, it revealed the coexistence of $Bi_2O_2CO_3$, g-C_3N_4 and Ag in this CN/Ag/BiOC system, which was in good agreement with the above analysis.

The UV–vis diffuse reflectance (UV–vis DRS) spectra of as-prepared samples were shown in Fig. 6. It could be seen that the absorption edge of the pure $Bi_2O_2CO_3$and g-C_3N_4occur at about 403 nm and 459 nm, respectively, which suggested that the $Bi_2O_2CO_3$ could only absorb UV light, while the g-C_3N_4 had strong absorption in visible light region. The absorption features of CN/BiOC and Ag/CN were similar to the g-C_3N_4, while the absorption intensities of both CN/BiOC and Ag/CN were stronger than the g-C_3N_4. The optical absorption of CN/Ag/BiOC shifted significantly to longer wavelengths and displayed higher absorption intensity over the range from 200 to 600 nm, in contrast with all other samples. This result was consistent with the literature [40]. According to the literature, the g-C_3N_4 could serve as an effective visible-light sensibilizer for $Bi_2O_2CO_3$. So this result may be mainly ascribed to synergic effect between the SPR of Ag metal and the addition of $Bi_2O_2CO_3$.

The photocatalytic activities of the as-preparedCN/Ag/BiOC composites were evaluated by photocatalytic removal of TC under the simulated solar light irradiation. As shown in Fig. 7a, in the absence of the photocatalyst, TC self-photodegradation was almost unobserved within 240 min, revealing that TC was quite stable toward incident light. The g-C_3N_4 exhibited the poorest catalytic activity among these catalysts and about 15% of TC was decomposed after irradiation for 240 min. Furthermore, it could be seen that CN/BiOC and CN/Ag/BiOC heterostructures all exhibited higher photocatalytic activity in the degradation of TC relative to the g-C_3N_4 sample. Specifically, the photocatalytic activities of CN/Ag/BiOC nanocomposites gradually increase with the weight of Ag from 1wt% to 4wt%. The decomposition rate would decrease again if more Ag was added into the CN/BiOC. Hence, the as-prepared 4wt%CN/Ag/BiOC nanocomposite was the optimal, and the maximum degradation effifficiency of 98.1% was attained after the irradiation for 240 min.

Following a Langmuir–Hinshelwood kinetic model, the photocatalytic degradation of TC at low concentrations followed the pesudo-fifirst-order kinetics. Figure 7b exhibited the photocatalytic degradation kinetics of TC and the 4wt% CN/Ag/BiOC nanocomposite possessed the optimum activity among all the samples with a rate constant of 29.5×10^{-3} min^{-1}, which was nearly 9 times that of pure g-C_3N_4 ($k = 0.032$ min^{-1}) and nearly 5 times that of g-C_3N_4/$Bi_2O_2CO_3$($k = 0.055$ min^{-1}).

The stability of the composite photocatalyst was evaluated by performing cycle experiments on the degradation of TC under simulated solar light irradiation, using 4wt% CN/Ag/BiOC. As shown in Fig. 8a, the photocatalytic efficiency showed very little variation after five successive cycles, which indicated that the CN/Ag/BiOC possessed excellent

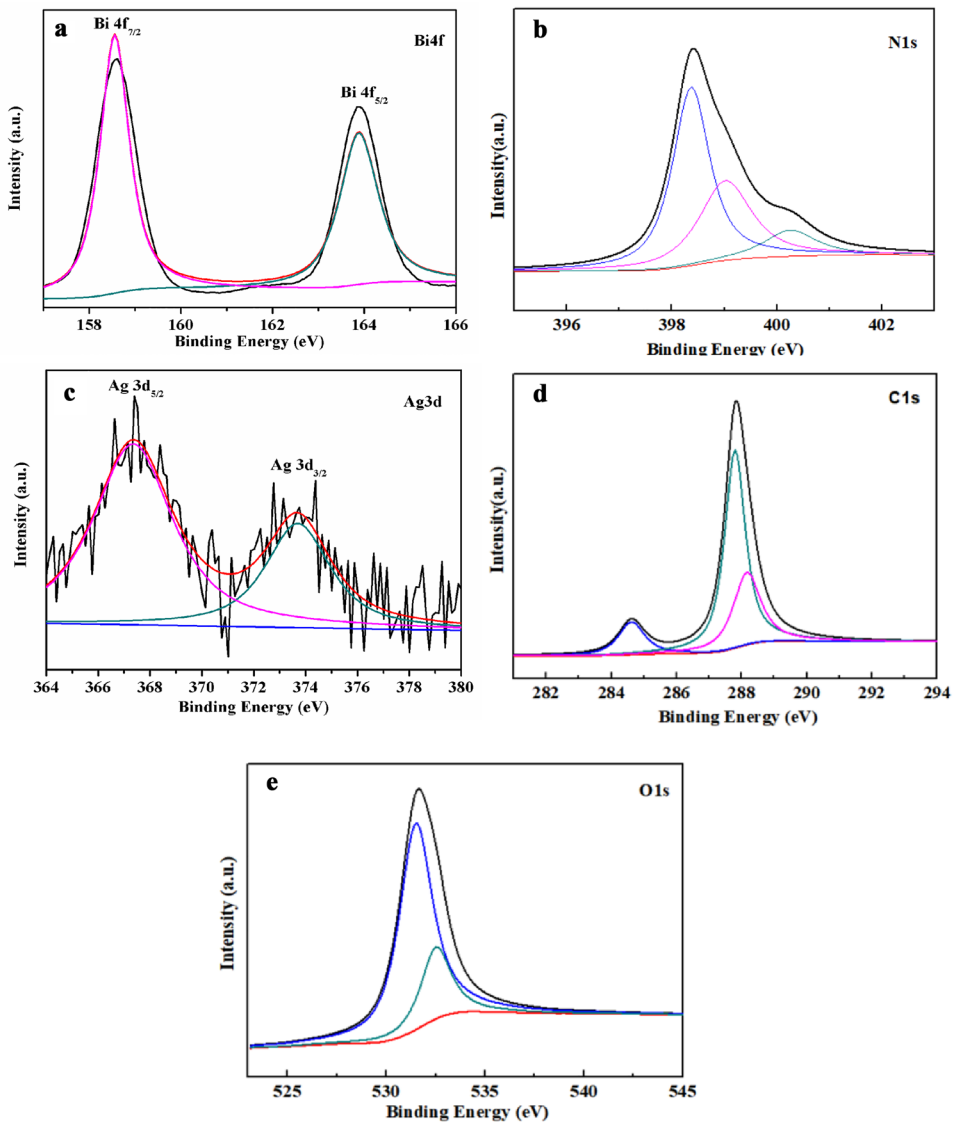

Fig. 5 XPS spectra of 4wt%CN/Ag/BiOC nanocomposites: **a** Bi 4f, **b** N 1s, **c** Ag 3d, **d** C 1s, and **e** O 1s

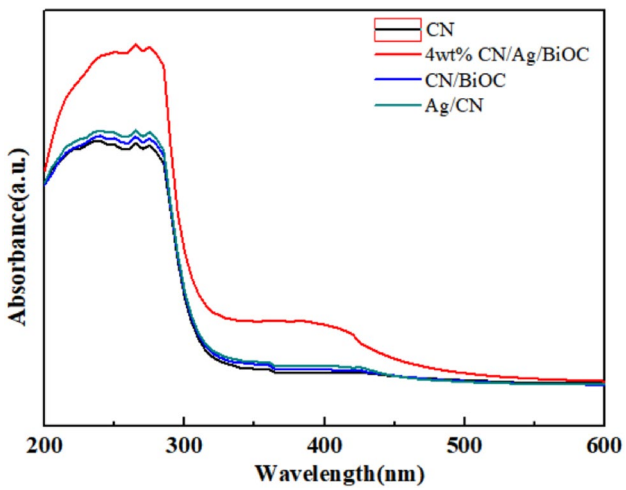

Fig. 6 UV–vis diffuse reflectance absorption spectra for the as-prepared samples

long term stability. These results suggested that the CN/Ag/BiOC were promising solar light photocatalyst for practical applications. Figure 8 (b) showed the XRD patterns of 4wt%CN/Ag/BiOC composite before and after five recycles for the photodegradation of TC under simulated solar light irradiation. It was obvious that the used 4wt%CN/Ag/BiOC composite showed similar XRD pattern compared to the fresh 4wt%CN/Ag/BiOC composite, which could prove the chemical stability of CN/Ag/BiOC photocatalyst in the photodegradation of TC solution.

Photoluminescence spectra (PL spectra) descend from the recombination of the free charge carriers. So the separation efficiency of the photogenerated electron–hole pairs of as-prepared composites were characterized by PL spectra. In generally, the higher the PL emission intensity indicated the higher the recombination of the photogenerated charge carriers and the lower the photocatalytic activity [49]. The

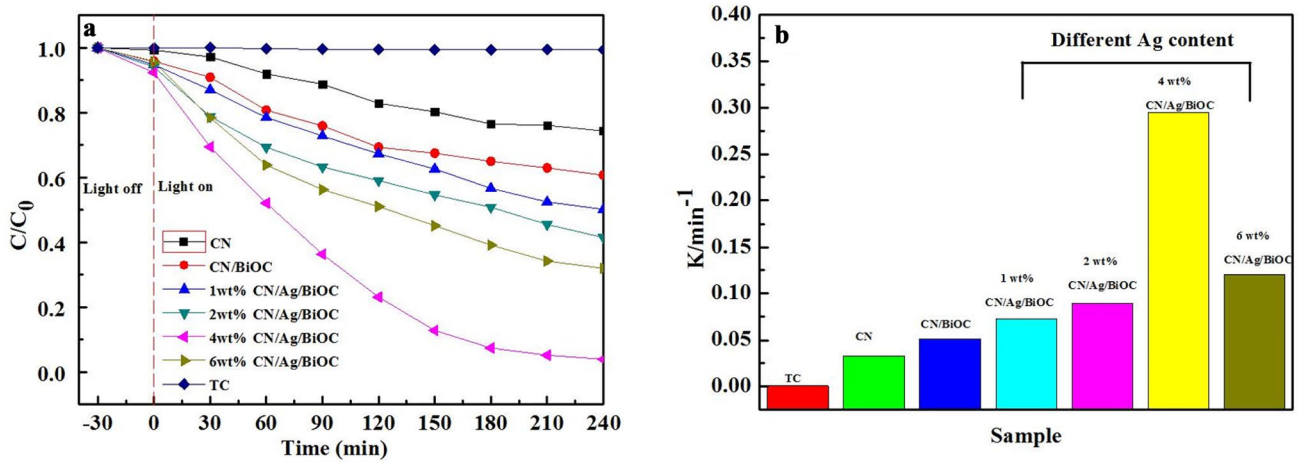

Fig. 7 **a** Photocatalytic degradation of TC under simulated solar lightirradiation using various catalysts. **b** The degradation rate constant of TC over various catalysts(amount of photocatalyst: 0.1gL^{-1}, TCconcentration: 10 mg L.$^{-1}$, pH: 7, and irradiation time: 120 min)

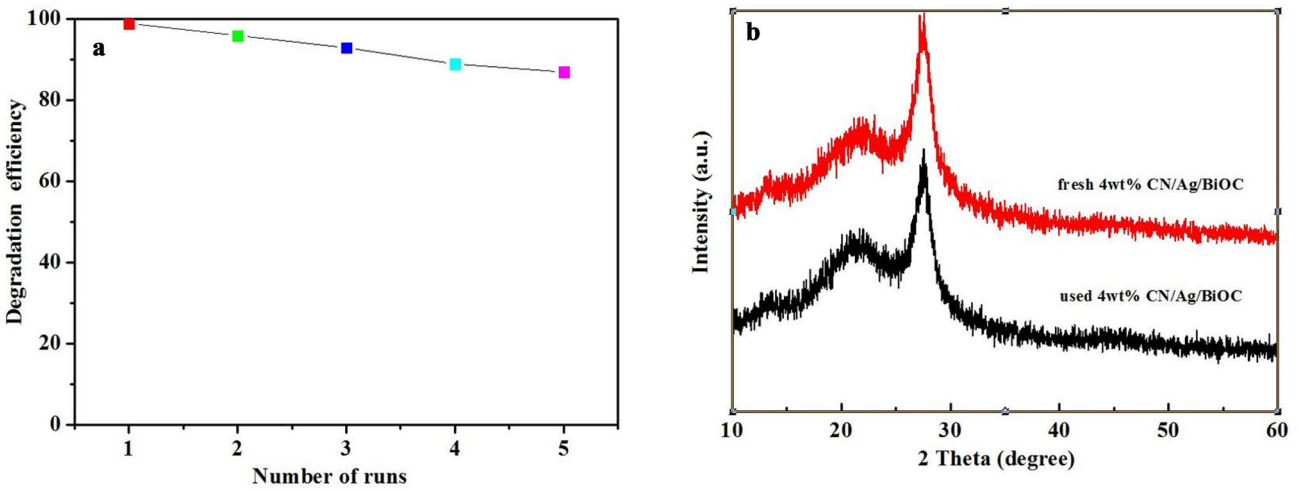

Fig. 8 **a** Recycling test on 4wt%CN/Ag/BiOC nanocomposites for the degradation of TC. **b** The XRD patterns of the fresh and used 4wt%CN/Ag/BiOC(amount of photocatalyst: 0.1gL^{-1}, TCconcentration: 10 mg L^{-1}, pH: 7, and irradiation time: 120 min)

PL spectra of g-C_3N_4, Ag/CN, CN/BiOC and 4wt%CN/Ag/BiOC at the excitation wavelength of 368 nm are shown in Fig. 9a. It was obvious that the g-C_3N_4 exhibited the highest intensity among all the samples. When the g-C_3N_4 combined with Ag and $Bi_2O_2CO_3$, the intensity of the PL emission decreased. The 4wt%CN/Ag/BiOC exhibited the lowest intensity which was consistent with its best degradation efficiency. Therefore, incorporation of Ag and $Bi_2O_2CO_3$ nanoparticles on the surface of g-C_3N_4 was highly favorable for efficient separation of photoinduced charge carriers, and thereby improves the photocatalytic activity of g-C_3N_4. Photoelectrochemical (PEC) experiment was accomplished to perform light-induced electron migration property. Transient photocurrent of g-C_3N_4, Ag/CN, CN/BiOC and 4wt% CN/Ag/BiOC were shown in Fig. 9b. As revealed in Fig. 8b, the 4wt% CN/Ag/BiOC possessed the highest photocurrent intensity, in which the enhanced photocurrent exemplified the higher separation of charge carriers. Meanwhile, these samples were tested by electrochemical impedance spectra (EIS) to investigate charge transfer rates. The EIS plots (Fig. 9c) illustrated that 4wt% CN/Ag/BiOC sample presented a relatively smaller arc radius of EIS Nyquist plot compared with the other samples, suggesting the relatively faster charge transfer in the 4wt% CN/Ag/BiOC sample. In other words, the 4wt% CN/Ag/BiOC exhibited lower resistance than the other samples and could facilitate the separation and immigration of photogenerated carriers under the light irradiation.

Figure 10a was a histogram of the effect of different scavengers on the photocatalytic process. The degradation

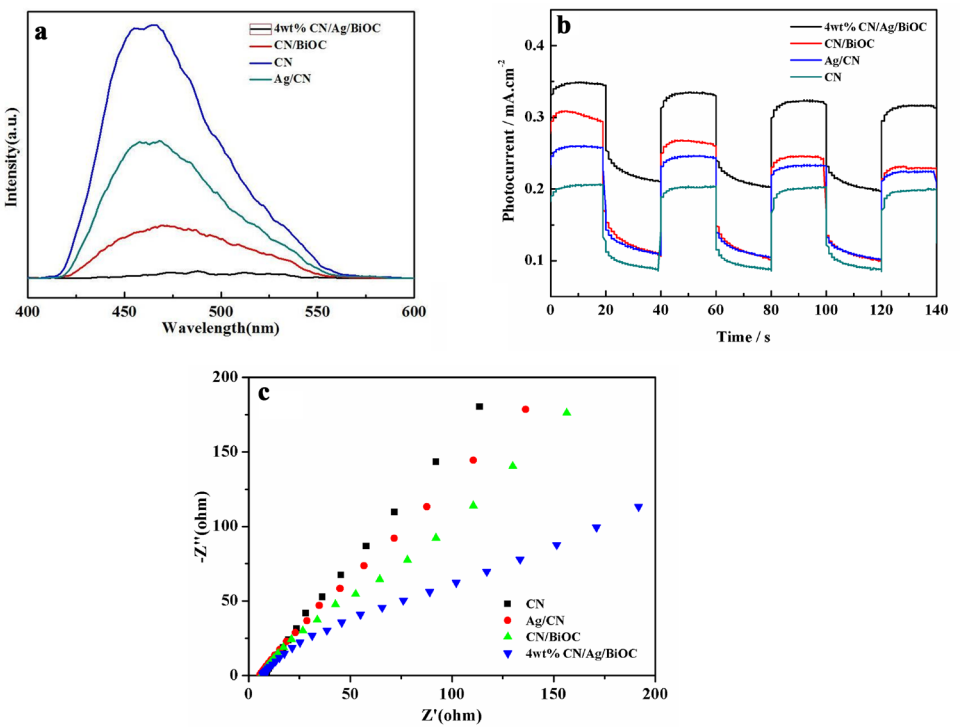

Fig. 9 **a** PL spectra; **b** Photocurrent transient and **c** Nyquist plots for as-prepared samples under simulated solar light irradiation

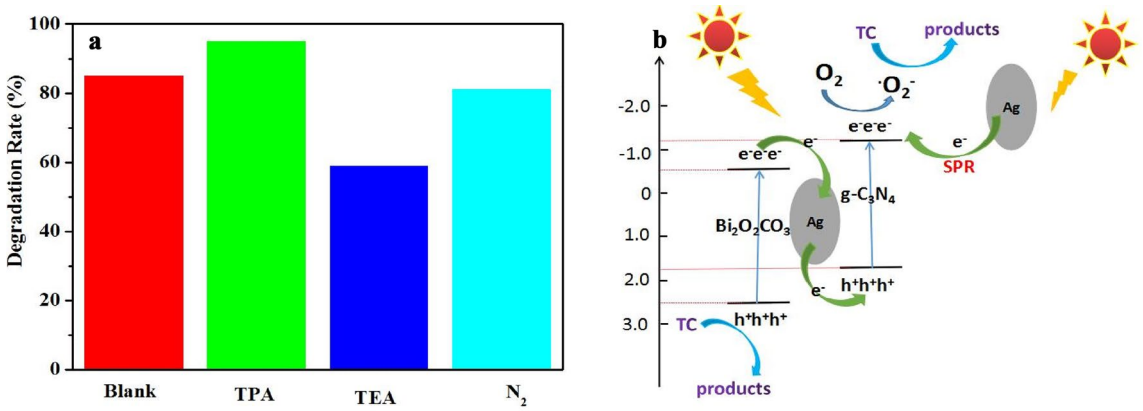

Fig. 10 **a** The histograms of different scavengers on photocatalytic reaction effect about 4wt%CN/Ag/BiOC; **b** the schematic of the separation and transfer of photogenerated charges over CN/Ag/BiOC with the possible reaction mechanism of photocatalytic procedure

rates of TC were drastically reduced after adding TEMPOL ($\cdot O_2^-$ scavenger). When the formic acid (h^+ scavenger) was added to the solution, the degradation rates of TC were slightly reduced. But the degradation rates of TC was enhanced in the presence of isopropanol ($\cdot$OH scavenger). This may have been attributed to the isopropanol greatly promoting the separation efficiency of electrons. Then, more electrons combined with O_2 to form $\cdot O_2^-$, leading to increased degradation activity [48]. Compared with those without any scavenger, the degradation rate decreased from 88 to 78%, 59%, respectively, which indicated that $\cdot O^{2-}$ is mainly responsible for this photocatalytic reaction.

According to the above results and some previous literature [27], a possible mechanism for the photocatalytic degradation of TC over CN/Ag/BiOC nanocomposites was proposed (Fig. 10b). As shown in Fig. 10b, the band-edge positions of the conduction band (CB) and the valence band (VB) of g-C_3N_4 were approximate − 1.13 eV and 1.57 eV, respectively, which could be known according to the results in the previous reports [27]. Correspondingly, the band-edge positions of CB and VB of $Bi_2O_2CO_3$ were around 0.50 eV and 2.58 eV, respectively [50]. When the heterojunction CN/Ag/BiOC were exposed to the simulated solar light, the electrons in the VB of g-C_3N_4 and $Bi_2O_2CO_3$ were excited

to the CB. The CN/Ag/BiOC was Z-scheme heterojunction and Ag NPs were paired between $Bi_2O_2CO_3$ and g-C_3N_4. The CB potential of $Bi_2O_2CO_3$ was more negative than that of Ag due to its high Schottky barriers at the interface of the semiconductor–metal, thus the photoinduced electrons of $Bi_2O_2CO_3$ would shift to metallic Ag and combined with the holes of g-C_3N_4. The electrons of $Bi_2O_2CO_3$ and holes of g-C_3N_4 would annihilate in Ag NPs. This electron increased the separation rate of photogenerated electron–hole pairs and prolongs the lifetime of free electrons and holes. Meanwhile, the surface plasmon resonance (SPR) effect of Ag nanoparticles enhanced the adsorption of light and rapid separation and transportation of photogenerated electrons-holes. Moreover, the photogenerated electrons on the CB of g-C_3N_4 captured O_2 to produce $\bullet O_2^-$ and then the $\bullet O_2^-$ oxidized the TC organic molecule. The holes on the VB of $Bi_2O_2CO_3$ could degrade TC organic molecule through direct oxidation. Therefore, CN/Ag/BiOC composites possess ed higher photocatalytic activity than the $Bi_2O_2CO_3$ and g-C_3N_4.

4 Conclusion

In summary, we had constructed a new type of CN/Ag/BiOC composite photocatalyst through a simple one-country synthesis strategy. It was found that the photocatalytic activity of CN/BiOC under simulated solar light was significantly enhanced after the introduction of Ag nanoparticles. When the weight content of Ag was 4%, the photocatalytic activity of CN/Ag/BiOC was optimum. In addition, the mechanism of photocatalytic degradation, UV–vis DRS, PL spectroscopy were studied. These results indicated that the matching conduction band levels of g-C_3N_4 and $Bi_2O_2CO_3$ and the surface plasmon resonance (SPR) effect of Ag nanoparticles led to enhanced light adsorption capacity of the catalyst, and the separation of photogenerated electron–hole pairs was accelerated. This work provided a new strategy for the degradation of tetracycline (TC) by ternary plasma photocatalysts.

Acknowledgements This work was supported by Shandong Provincial Natural Science Foundation (ZR2020MB036)

Declarations

Conflict of interest The authors declare that they have no conflict of interest.

References

1. Qian X, Xu L, Zhu Y, Yu H, Niu J (2021) Chem Eng J 420:127615–127620
2. Zhou C, Lai C, Huang D, Zeng G, Zhang C, Cheng M, Hu H, Wan J, Xiong W, Wen M, Wen X, Qin L (2018) Appl Catal B Environ 220:202–210
3. Müller A, Xu Z, Greiner A (2022) Mater Eng 307:2200238–2200245
4. Alazaiza M, Albahnasawi A, Copty N, Ali G, Bashir M, Abu A, Abushammala M, Nassani D, Maskari T (2022) Global NEST J 24(1):74–86
5. Pang S, Lin Z, Li J, Zhang Y, Mishra S, Bhatt P, Chen S (2022) Front Microbiol 13:713375–713381
6. Jin B, Cho Y, Zhang Y, Li P, Zhan K, Lee KS, Park JH (2019) Nano Energy 66:104110–104118
7. Chandrasekaran S, Chung J, Kim E, Hur S (2016) Chem Eng J 290:465–476
8. Fu J, Bie C, Cheng B, Jiang C, Yu J (2018) ACS Sustain Chem Eng 6:2767–2779
9. Liu C, Zhang Y, Dong F, Reshak A, Ye L, Pinna N, Zeng C, Zhang T, Huang H (2017) Appl Catal B Environ 203:465–474
10. Zhu B, Zhang L, Cheng B, Yu J (2018) Appl Catal B Environ 224:983–999
11. Mamba G, Mishra A (2016) Appl Catal B Environ 198:347–377
12. Wang L, Wang C, Hu X, Xue H, Pang H (2016) Chem–An Asian J 11: 3305–3328
13. Zhang H, Guo L, Zhao L, Wan B, Yang Y (2015) J Phys Chem Lett 6:958–963
14. Lin Q, Li L, Liang S, Liu M, Bi J, Wu L (2015) Appl Catal B Environ 163:135–142
15. Yan J, Zhou C, Li P, Chen B, Zhang S, Dong X, Xi F, Liu J (2016) Colloid Surface A 5:257–264
16. Luo L, Zhang A, Janik M, Li K, Song C, Guo X (2017) Mater Lett 188:130–133
17. Wang X, Chen X, Thomas A, Fu X, Antonietti M (2009) Adv Mater 21:1609–1612
18. Meng J, Lan Z, Chen T, Lin Q, Liu H, Wei X, Lu Y, Li J, Zhang Z (2018) J Phys Chem C 122:24725–24731
19. Maeda K, Wang X, Nishihara Y, Lu D (2009) J Phys Chem C 113:4940–4947
20. Sun J, Zhang J, Zhang M, Antonietti M, Fu X, Wang X (2012) Nat Commun 3:1139–1144
21. Zheng J, Jiao Z (2017) J Coll Inter Sci 488:234–239
22. Zheng J, Jiao Z (2017) J Coll Inter Sci 504:620–625
23. Duan Y, Yao H, Li J, Shang X, Jia D, Li C (2019) Water Sci Technol 146:1494–1502
24. Yu L, Zhang X, Li G, Cao Y, Shao Y, Li D (2016) Appl Catal B 187:301–309
25. Wang Q, Yun G, Bai Y, An N, Lian J, Huang H, Su B (2014) Appl Surf Sci 313:537–544
26. Hu D, Zhang K, Yang Q, Wang M, Xi Y, Hu C (2014) Appl Surf Sci 316:93–101
27. Zhang Z, Lin S, Cui W, Li X, Li H (2019) Mater Lett 234:264–268
28. Hu R, Xiao X, Tu S, Zuo X, Nan J (2015) Appl Catal B 163:510–519
29. He Y, Zhang L, Teng B, Fan M (2015) Environ Sci Technol 49(1):649–656
30. Chen Y, Zhao C, Ma S, Xing P, Hu X, Wu Y, He Y (2019) Inorg Chem Front 6:3083–3092
31. Chen P, Chen L, Ge S, Zhang W, Wu M, Xing P, Rotamond TB, Lin H, Wu Y, He Y (2020) Int J Hydrogen Energy 45(28):14354–14367
32. Chen L, Wang J, Li X, Zhao C, Hu X, Wu Y, He Y (2022) Inorg Chem Front 9:2714–2724
33. Di J, Xia J, Ji M, Wang B, Yin S, Huang Y, Chen Z, Li H (2016) Appl Catal B-Environ 188:376–387
34. Qua S, Xiong Y (2018) J Photoch Photobio A 365:23–31
35. Gao X, Shang Y, Liu L, Nie W (2019) Opt Mater 88:229–237
36. Dong F, Zhao Z, Xiong T, Ni Z, Zhang W, Sun Y, Ho W (2013) ACS Appl Mater Interfaces 5:11392–11401
37. Ma Y, Bian Y, Tan P, Shang Y, Liu Y, Wu L, Zhu A, Li W, Xiong X, Pan J (2017) J Colloid Interf Sci 497:144–154

38. Meia F, Daia K, Zhang J, Li W, Liang C (2019) Appl Surf Sci 488:151–160
39. Li Y, Zhan J, Huang L, Xu H, Li H, Zhang R, Wu S (2014) RSC Adv 4:11831–11839
40. Tian N, Huang H, Guo Y, He Y, Zhang Y (2014) Appl Surf Sci 322:249–254
41. Zhang Q, Wang H, Hu S, Lu G, Bai J, Kang X, Liu D, Gui J (2015) RSC Adv 5:42736–42743
42. Yang M, Hu S, Li F, Fan Z, Wang F, Liu D, Gui J (2014) Ceram Int 40:11963–11969
43. Jiang W, Luo W, Zong R, Yao W, Li Z, Zhu Y (2016) Small 12:4370–4378
44. Wang X, Fan H, Ren P, Yu H, Li J (2012) Mater Res Bull 47:1734–1741
45. Wang S, Li D, Sun C, Yang S, Guan Y, He H (2014) Appl Catal B Environ 144:885–891
46. Martha S, Nashim A, Parida K (2013) J Mater Chem A 1:7816–7823
47. Xu J, Harmer J, Li G, Chapman T, Collier P, Longworth S (2010) Tsang S 46:1887–1889
48. Jiang J, Gao J, Li T, Chen Y, Wu Q (2019) XieT, Lin Y, Dong S. J Colloid Interf Sci 554:531–543
49. Hong Y, Li C, Fang Z, Luo B, Shi W (2017) Carbon 121:463–471
50. Yang C, Xue Z, Qin J, Sawangphruk M, Rajendran S, Zhang X, Liu R (2019) J Phys Chem C 123:4795–4804

Authors and Affiliations

Jingjing Zheng[1] · Guoxia Liu[1] · Xiaozheng Feng[1] · Zhengbo Jiao[2]

✉ Jingjing Zheng
zjj65050@163.com

✉ Zhengbo Jiao
jiaozhb@qdu.edu.cn

[1] Department of Chemical Engineering and Safety, Binzhou University, Binzhou 256603, China

[2] Institute of Materials for Energy and Environment, Qingdao University, Qingdao 266071, China